# Comprehensive characterization and development of multi-core shell superparamagnetic nanoparticles for controlled delivery of drugs and their kinetic release modelling

Simone Moretto [a,b,c,1], Adriano Santos Silva [a,b,d,e,*,1], Jose L. Diaz de Tuesta [f,**], Fernanda F. Roman [a,b,d,e], Rita Cortesi [c], Ana Raquel Bertão [g], Manuel Bañobre-López [g], Marta Pedrosa [d,e], Adrián M.T. Silva [d,e], Helder T. Gomes [a,b]

[a] Centro de Investigação de Montanha (CIMO), Instituto Politécnico de Bragança, Campus de Santa Apolónia, 5300-253, Bragança, Portugal
[b] Laboratório Associado para a Sustentabilidade e Tecnologia em Regiões de Montanha (SusTEC), Instituto Politécnico de Bragança, Campus de Santa Apolónia, 5300-253, Bragança, Portugal
[c] Dipartimento di Scienze Chimiche, Farmaceutiche e Agrarie, Università degli Studi di Ferrara, 44121, Ferrara, Italy
[d] LSRE-LCM - Laboratory of Separation and Reaction Engineering – Laboratory of Catalysis and Materials, Faculty of Engineering, University of Porto, Rua Dr. Roberto Frias, 4200-465, Porto, Portugal
[e] ALiCE - Associate Laboratory in Chemical Engineering, Faculty of Engineering, University of Porto, Rua Dr. Roberto Frias, 4200-465, Porto, Portugal
[f] Chemical and Environmental Engineering Group, ESCET, University Rey Juan Carlos, C. Tulipán s/n, 28933, Móstoles, Spain
[g] Advanced (Magnetic) Theranostic Nanostructures Lab, International Iberian Nanotechnology Laboratory, Av. Mestre Jose Veiga s/n, 4715-330, Braga, Portugal

## ARTICLE INFO

## ABSTRACT

The nanoparticles designed for application in cancer treatment should have biocompatibility, colloidal stability and triggered release at tumor sites. Magnetic nanoparticles arise as an interesting option to be used as drug nanocarriers, considering the possibility of driving nanoparticles to the correct delivery site and exploring different triggers to achieve such accomplishment. In this study, nickel ferrite nanoparticles are explored as a magnetic core for drug delivery systems, using doxorubicin and omeprazole as model drugs. The developed nickel ferrite presents a strong superparamagnetic behavior and high purity, as demonstrated by magnetometry and TGA results. The carbon-coating procedure and functionalization allowed the nanoparticle to achieve the desired characteristics for biomedical applications (*i.e.* stability in water, biocompatibility, and size). According to TEM results, the final carbon-coated magnetic nanoparticles have an average size of 25.09 ± 0.58 nm and multi-core shell architecture, which is suitable for biomedical applications as drug nanocarriers. In addition, DLS demonstrated that functionalized nanoparticles are monodisperse, with a hydrodynamic diameter of 167 ± 59 nm, which fits the recommended range (100–200 nm) to benefit from enhanced permeability and retention effect. Drug loading tests with doxorubicin and omeprazole revealed the versatility of the designed nanoparticles, able to load 97% of doxorubicin and 51% of omeprazole. The pH-triggered release was also confirmed for both pharmacological compounds, showing a higher cumulative drug under acidic conditions (simulating a tumor microenvironment). Finally, the kinetic analysis applied to the study of the release mechanism of both medicines showed that non-linear models fit with higher accuracy the experimental data.

## 1. Introduction

The typical protocol for treating solid tumors currently involves surgical resection followed by chemotherapy or radiotherapy to kill the residual cancer cells [1]. However, the main limitation of chemotherapy is the significant systemic toxicity of the employed agents owing to their low tissue specificity and the narrow therapeutic index. A possible solution is developing a drug delivery system carrying the medicament

---

directly to the malignancy tissue [2]. Nanoparticles are considered potential carriers of pharmacological compounds for drug delivery systems due to their peculiar physicochemical properties and because they can be designed with different materials, architectures and properties [3,4]. Nanoparticles showing magnetic behavior offer a promising approach to drug delivery since they can be driven and fixed to the tumor site using an external magnetic field [5]. Such an approach, named Magnetic Drug Targeting (MDT), can reduce the dosage required and prevent side effects resulting from the site-specific release of the medication [6]. In the last few years, the utilization of magnetic nanoparticles for cancer treatment has advanced significantly, including practical applications [7–16].

Over the past decades, many magnetic nanocarriers have been developed, such as magnetic yolk-shell and multi-core shell nanoparticles [17,18]. The main feature of magnetic yolk-shell nanoparticles is the void between the inner magnetic core and the surrounding shell, which makes them particularly suitable for MDT because drugs can be loaded inside the void. However, the synthesis procedure of the nanoparticles can be exhaustive, decreasing the feasibility of their utilization in real scenarios. On the other hand, magnetic multi-core shell nanoparticles (MMCSNPs) can also be used for the same purpose, considering the synthesis of porous shells and using interstitial space between the cores. At the same time, the shell can be designed to meet the needs of biocompatibility and colloidal stability [17,19]. To be applied as MDT nanocarriers, magnetic nanoparticles must be superparamagnetic. Superparamagnetism is a form of magnetism that appears in nanoscale ferromagnetic materials, and it is characterized by high magnetic saturation and no coercivity [20]. Such features are essential because they guarantee that the external magnetic field easily drives the nanoparticles and that they revert to a nonmagnetic state when the field is removed [21,22]. Most studies consider the utilization of magnetite ($Fe_3O_4$) or maghemite ($\gamma$-$Fe_2O_3$) for the superparamagnetic core [23]. However, the partial oxidation of the materials can lead to magnetic activity loss. On the other hand, ferrites arise as an interesting option for magnetic materials to be used for MDT purposes, but few studies explore their performance for this application. For instance, nickel ferrite is arousing interest in MDT as it shows a high magnetic responsive behavior at room temperature [24].

The synthesis of MMCSNPs is a complex stepwise pathway that starts with fabricating the magnetic core. Sol-gel synthesis is particularly advantageous in the preparation of magnetic cores. The low temperature of processing and the high control over the final nano-products' structure, size and purity make the sol-gel route a versatile and cost-effective methodology [25]. To obtain magnetic material via sol-gel, inorganic metal salt or metal alkoxide precursors undergo hydrolysis and condensation reactions in the presence of capping and chelating agents that drive the nucleation and the growth phases to obtain small and homogeneous particles [26]. The second step is preparing the porous shell, frequently realized by the harsh template strategy. This template approach covers the nanocores with a transitory scaffold layer of solid material, such as silica, polymers or carbon, on which the shell layer is synthesized [17]. Subsequently, the scaffold is selectively removed by etching, dissolution or calcination, obtaining the pores in the carbon shell and cleaning the interstitial spaces in the cores [27].

The design and preparation of the shell of nanoparticles are crucial for *in vivo* applications to ensure the final nanoproduct is stable, nontoxic and biocompatible [28]. Shell surfaces can be functionalized with polymers to improve biocompatibility, prevent aggregation and also protect the core from the degradation and leaching of toxic metal ions [29]. Mesoporous carbons are great materials for constructing a porous shell capable of adsorbing large amounts of drugs for anticancer drug delivery [30]. The MDT based on carbon shell nanoparticles is a tissue-specific drug delivery system that brings and accumulates medicaments inside the tumor. Despite the significant results reported in the literature for applying carbon-based superparamagnetic nanoparticles for drug delivery purposes, most works do not show a detailed

characterization of them, even less during their synthesis steps [31,32]. For instance, a detailed description of the samples throughout the synthesis procedure could reveal the mechanisms behind each synthesis step, allowing a more thoughtful design of new nanocarriers. In addition, coating other magnetic cores with traditional carbon-coating methodologies [31–34] could indicate whether the coating procedure is sensitive towards other magnetic cores and give further insights into the versatility of the coating procedure.

Several studies reported in the literature are devoted to the development of nanoparticles for magnetic drug targeting to deliver doxorubicin (DOX). DOX is a chemotropic agent for treating solid tumor-like bladder and breast cancer [35]. It works by interfering with the function of the DNA to force the cancer cell to activate apoptotic suicide [35]. However, its pharmacologic action is hindered by the cellular endosomes that sequester the drug from the cytosolic environment [36]. Therefore, proton-pump inhibitors like omeprazole (OME), typically employed in treating gastroesophageal diseases, are interesting molecules to sabotage the endosomal internalization mechanism supporting the DOX effectiveness [37]. For instance, there are no works dealing with the development of magnetic nanoparticles for MDT studies of OME. Another important evaluation to increase the MDT approach's viability is pharmacokinetics. The study begins by comprehending the mass transference mechanisms involved in drug release and exploring models to predict drug release amounts. In the last few years, many mathematical methods have been proposed to design simple and complex drug delivery systems and predict the overall release behavior [38]. Comprehending the parameters used in the different models to fit drug release data reveals important physical characteristics regarding the drug release profile. For instance, most studies dealing with DOX release do not study the release profile with the aid of mathematical models or even lack proper mathematical sensitivity (*i.e.* constants are presented without unities) [32,39]. The lack of proper kinetic studies represents a fundamental literature gap to be fulfilled.

This work aims to show a detailed characterization throughout the synthesis procedure to obtain MMCSNPs architecture. In addition, the traditional resorcinol/formaldehyde carbon coating was employed, considering nickel ferrite as the magnetic core, prepared by sol-gel methodology. The detailed characterization presented here during the synthesis steps demonstrates the mechanisms involved in each step, which can help further developments in nanoparticle design for biomedical applications. MMCSNPs were functionalized with nitric acid and Pluronic® F-127 to obtain a negatively charged surface and increase the colloidal stability in a hydrophilic environment. The coating and functionalization procedure ensures the obtention of a biocompatible nanoparticle, as demonstrated in previous works using a similar methodology for the synthesis of carbon-based magnetic nanoparticles [32]. Moreover, their application as drug nanocarriers for MDT was investigated, studying their ability to load active substances and deliver them with a pH-dependent release profile. For this purpose, DOX and OME were chosen for the drug delivery tests, carried out in physiological (pH 7.4), tumor (pH 6.0), and endosome/lysosome microenvironment (pH 4.5). The release mechanism was further investigated by fitting experimental drug release data using six kinetic models: zero-order, first-order, Higuchi, Korsmeyer-Peppas, Hixon-Crowell, and Weibull models.

## 2. Methods

### 2.1. Chemicals

Iron (III) nitrate nonahydrate ($Fe(NO_3)_3 \cdot 9H_2O$, 99%) and ammonia ($NH_4OH$, 28–30% in $H_2O$) were purchased from Merk. Sodium hydroxide (NaOH, 99%) and nickel (II) nitrate hexahydrate ($Ni(NO_3)_2 \cdot 6H_2O$, 99%) were obtained from VWR Chemicals. Ethanol absolute ($CH_3CH_2OH$, 96%) and nitric acid ($HNO_3$, 65% in $H_2O$), were supplied from Fisher Chemicals, whereas Pluronic® F-127, ($C_3H_6O \cdot C_2H_4O)_x$, and ethylene glycol ($HOCH_2CH_2OH$, 99.5 wt%), from Sigma-

Aldrich. Resorcinol ($C_6H_4$-1,3-$(OH)_2$, 99.8%), tetraethyl orthosilicate (TEOS, $Si(OC_2H5)_4$, 98%) and formaldehyde (HCHO, 37% in $H_2O$) were purchased from Alfa Aesar, Fluka and Pancreac, respectively. Doxorubicin hydrochloride ($C_{27}H_{29}NO_{11}$·HCl, 98%) was purchased from Discovery Fine Chemicals and omeprazole ($C_{17}H_{19}N_3O_3S$, >99%) was purchased from Acros Organics. All aqueous solutions were prepared using deionized water (18.2 MΩ cm at 25 °C), produced in a Milli-Q system (Millipore). All reagents were used as received without further purification.

## 2.2. Synthesis of MMCSNPs

The preparation of MMCSNPs with a nickel ferrite core and a carbon shell functionalized for biomedical application as MDT systems consisted of five main phases, schematically illustrated in Fig. 1: (1) Sol/Gel synthesis of nickel ferrite core, (2) coating of cores, (3) carbonization, (4) silica etching and (5) surface functionalization.

### 2.2.1. Synthesis of magnetic nickel ferrite core

The synthesis of magnetic nickel ferrite (NiFe) nanosized cores was done through a sol-gel method following the protocol of *Giannakopoulou* et al. [40]. Briefly, 10 mL of a 1 M $Ni(NO_3)_2$6$H_2O$ solution prepared in ethanol was mixed with 40 mL of a 0.5 M solution of $Fe(NO_3)_3$9$H_2O$ and ethyl glycol. Afterwards, the solution was stirred at 60 °C for 2 h to sustain the transition from the sol to the gel state. Finally, the temperature was increased to 220 °C until the complete drying of the gel. To reach the proper crystal structure, the dark gray powder obtained underwent a high-temperature treatment (12 h at 300 °C, 24 h at 600 °C and 1 h at 1000 °C), resulting in the NiFe sample.

### 2.2.2. Multi-core shell architecture

Carbon multi-core shell architecture was built via the harsh template method, adapting the protocol described by *Lie* et al. [41] that consists of two steps. NiFe (cores) was coated with a layer of silica and phenolic resin (PhR) in the first step. In brief, a sonicated suspension was made of 0.25 g of NiFe, 50 mL of distilled water, 1.3 mL of ammonia and 150 mL of ethanol, and then mixed at 30 °C for 1 h. Subsequently, 210 μL of TEOS and 150 μL of formaldehyde were added dropwise. Then, the reaction was stirred at 30 °C for 6 h and lastly, the temperature was increased to 80 °C and maintained for 8 h. The final product denoted as NiFe@$SiO_2$/PhR was centrifuged, washed and dried at 60 °C overnight. The second step involves the annealing of the nanoparticles and the silica etching. The annealing was performed in a tubular vertical furnace under an $N_2$ flow (100 Ncm$^3$ min$^{-1}$), setting the following heating program: 120 °C for 1 h, 400 °C for 1 h and 600 °C for 4 h, with a heating ramp of 2 °C min$^{-1}$, allowing the carbonization of the PhR and leading to NiFe@$SiO_2$/C. Afterwards, the silica was etched by pouring NiFe@$SiO_2$/C in a 10 M sodium hydroxide solution for 16 h at room temperature. The sample was extensively washed with distilled water until neutrality of the rinse waters and dried overnight at 60 °C in an air oven. The obtained MMCSNPs were denoted as NiFe@C.

### 2.2.3. Surface functionalization

Two surface treatments were performed to increase the colloidal stability of NiFe@C in a hydrophilic body environment and increase their biocompatibility. The first was the carbon surface oxidation of 5
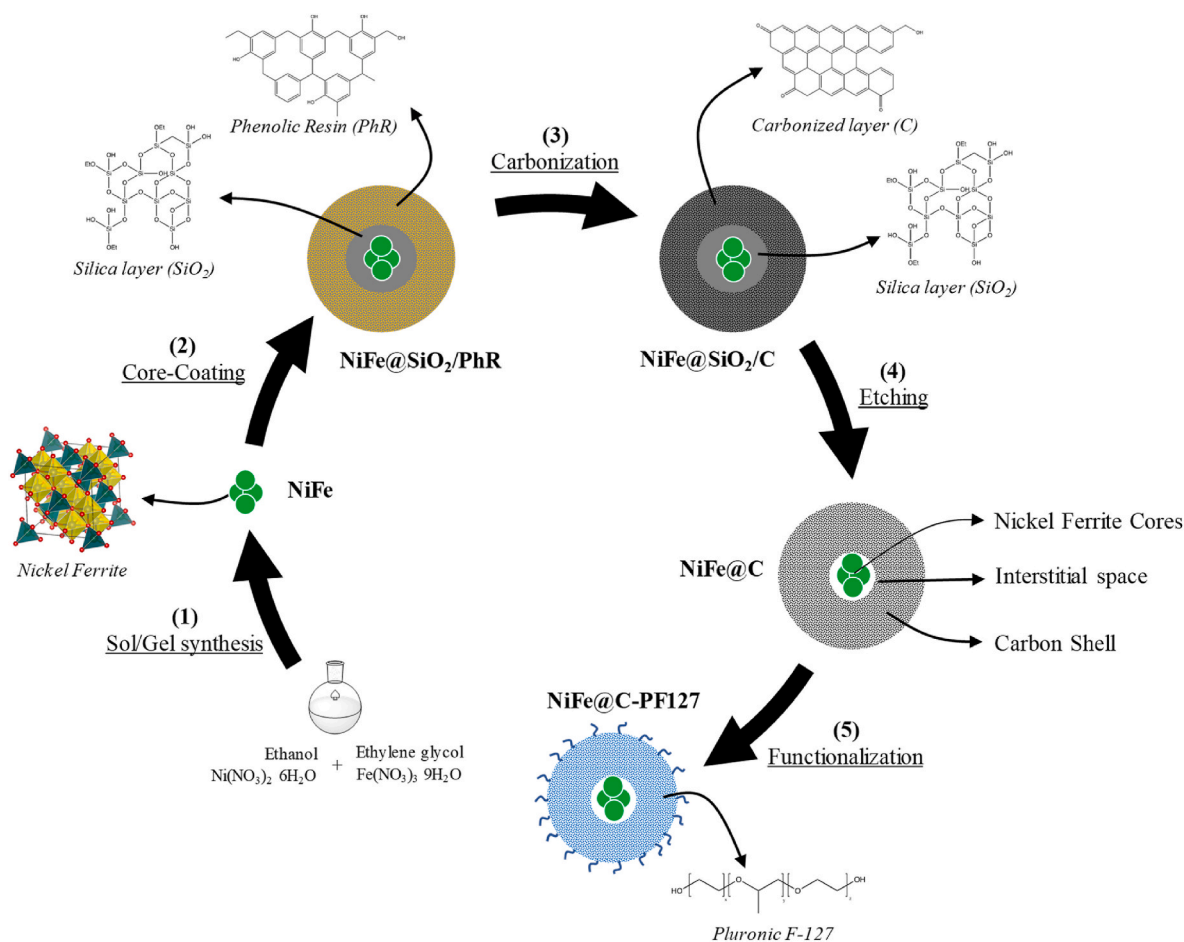


**Fig. 1.** Schematic illustration of the five main phases constituting the synthetic pathway of magnetic multi-core shell nanoparticles with a nickel ferrite core and a mesoporous carbon shell. 35.

mg mL$^{-1}$ NiFe@C using nitric acid (1 M) at 65 °C under stirring for 3 h, leading to NiFe@C-ox. The second step was the functionalization of NiFe@C-ox with the biocompatible polymer Pluronic® F-127. For this purpose, 100 mg of the nanoparticles were mixed with 50 mL of distilled water and 2 g of Pluronic® F-127 for 5 h at room temperature. The resultant product, NiFe@C-PF127, was separated by centrifugation and dried overnight at 60 °C in an air oven.

### 2.3. Physicochemical characterization of the nanomaterials

The NiFe sample was analyzed by X-ray diffraction (XRD) using a PANalyticalX'Pert PRO X-ray diffractometer equipped with a X'Celerator detector and secondary monochromator (Cu Kα λ = 0.154 nm). The result was further processed using X'Pert HighScore Plus software for crystalline phase identification. XRD data were further exploited to estimate the average size of the cores, applying mathematic methodologies, as described by Nath et al. [42]. The nanoparticles morphology (multi-core shell architecture and size) was examined by Transmission Electron Microscopy (TEM). TEM images were taken with a JEOL JEM 2100, operating at 200 kV. Firstly, the images were selected to choose the ones more representative of the bulk sample. Then, the contrast and brightness of the chosen images were adjusted to emphasize the particle boundaries from the background. Finally, particles were manually selected after the scale setting to build the histogram representing the distribution of nanoparticles' sizes found in the samples. Later, average diameters with their relative standard deviations were determined by fitting the histogram profile with the Gaussian function. The surface chemistry of the nanomaterials obtained after every synthesis step was followed by Fourier Transform Infrared Spectroscopy (FT-IR), performed with a PerkinElmer FT-IR spectrophotometer UATR Two with a resolution of 4 cm$^{-1}$ and a scan range of 4000 to 450 cm$^{-1}$. For FT-IR analysis, each sample was prepared by mixing *ca.* 1 mg of nanomaterial and 100 mg of KBr, pressed in a tablet. Thermogravimetric analysis (TGA) was performed with a STA 449 PC/4/H Luxx (Netzsch) to evaluate mass loss as a function of the temperature. For this purpose, NiFe, NiFe@SiO$_2$/C, and NiFe@C samples were analyzed under an air atmosphere (100 mLSTD min$^{-1}$) from 50 to 950 °C, with a heating rate of 10 °C min$^{-1}$. Elemental analysis (elemental analyzer from Elementar with a Rapid Oxy Cube module used to determine the oxygen content and a Rapid Micro Cube module for the quantification of carbon, hydrogen, nitrogen and sulfur) was also performed before and after thermal treatment for samples NiFe@SiO$_2$/PhR and NiFe@SiO$_2$/C to evaluate the carbonization degree during annealing. The superparamagnetic behavior of NiFe@C-PF127 MMCSNPs was verified with a superconducting quantum interference device (SQUID-VSM) magnetometer, recording the hysteresis curve at 300 K. N$_2$ adsorption/desorption isotherms were recorded in a Quantachrome NOVA 4200e adsorption analyzer at −196 °C to determine the Brunauer-Emmett-Teller specific surface area ($S_{BET}$), as described in previous works [43,44]. The zeta potential, the average hydrodynamic diameter of NiFe@C-PF127 and the polydispersity index (PDI) were determined upon analysis of dynamic light scattering (DLS) results obtained using a Horiba SZ-100Z.

### 2.4. Stability of the MMCSNPs

Considering the future application of the MMCSNPs as drug nanocarriers, it is important to evaluate its stability towards metal leaching from the MMCSNPs. In this regard, a test was performed under the same conditions to assess drug release capabilities. In brief, 2 mg of either the bare core (NiFe sample) or NiFe@C-PF127 were placed in 20 mL of PBS solutions 4.5, 6.0 and 7.4. The mixture remained under stirring for 48 h at 37 °C, and the supernatant was recovered to determine iron and nickel concentrations using atomic absorption spectroscopy (Varian SpectrAA 220).

### 2.5. Drug loading

The loading of either DOX or OME was performed by mixing 20 mL of 1 mg mL$^{-1}$ NiFe@C-PF127 suspension, sonicated for 30 min, with 20 mL of drug aqueous solution (0.5 and 0.3 mg mL$^{-1}$ for DOX and OME, respectively). Then, the loading system was stirred inside an orbital shaker at room temperature for 48 h and protected from the light. After this period, drug-loaded NiFe@C-PF127 were separated by centrifugation, washed, frozen and lyophilized overnight at 0.04 mbar and −46 °C. The same procedure was repeated without the MMCSNPs to evaluate the possible drug degradation during the loading runs. Additionally, the procedure was also performed in the absence of drugs (referred to as NiFe@C-PF127-empty). The supernatant was analyzed with a UV–Vis spectrophotometer at 480 nm and 300 nm for DOX and OME, respectively. The same procedure was repeated without the MMCSNPs to evaluate the possible drug degradation during the loading runs (negative control). The drug loading process was evaluated by calculating two parameters: Drug Loading Efficiency (DLE) and Drug Loading Capacity (DLC), as described in Eq. (1) and Eq (2), respectively.

$$DLE(\%) = \frac{C_i - C_f}{C_i} \times 100 \qquad \text{Eq. (1)}$$

$$DLC = \frac{M_d}{M_{np}} \qquad \text{Eq. (2)}$$

in the equations, $C_i$ and $C_f$ are the drug concentrations in the aqueous solution at the beginning and end of the drug loading process. $M_d$ is the mass of the drug loaded into NiFe@C-PF127, and $M_{np}$ is the mass of NiFe@C-PF127. The loading of either DOX or OME was repeated three times for statistical validation of the results. FT-IR analysis was carried out with drug-loaded nanoparticles and pure drugs to evaluate if the drug loading was efficient, following the same procedure used for the physicochemical characterization of nanoparticles.

### 2.6. Kinetic drug release

The particles' pH-dependent DOX and OME release profile was evaluated using the protocol described elsewhere [32]. Briefly, 2 mg of NiFe@C-PF127 loaded with DOX or OME were suspended in 20 mL of three different phosphate-buffered saline (PBS) solutions prepared using ultrapure water as the solvent at different pHs (7.4, 6.0 and 4.5). Release systems were protected from the light and incubated under agitation at 37 °C. At selected intervals (0.5, 1, 2, 4, 6, 24 and 48 h) from the beginning of the experiment, the PBS medium was separated from the NiFe@C-PF127 with the aid of a strong neodymium magnet, withdrawn and replaced with an equal amount of fresh PBS. This procedure ensures that mass transfer limitations will not interfere with drug release, so simulating the conditions faced in the real intravenous application of drug nanocarriers. The same procedure was repeated using nanoparticle NiFe@C-PF127-empty for all pH values to ensure that no possible leaching was being accounted as drugs released (no significant response was observed). The samples were analyzed with a UV–Vis spectrophotometer at 480 nm and 300 nm to determine the desorbed amount of DOX and OME, respectively. Results were expressed in terms of average value of *percentage cumulative drug release* (CDR) calculated on three independent experiments, as defined in Eq. (3) and Eq (4).

$$CDR_t(\%) = \frac{\sum\limits_{t=0.5}^{t} M_t}{DLC_{2\,mg}} \times 100 \qquad \text{Eq. (3)}$$

$$DLC_{2mg}(mg) = \frac{DLC \times 2\,mg}{DLC + 1} \qquad \text{Eq. (4)}$$

$CDR_t$ (%) represents the percentage of the total amount of drug desorbed from the beginning of release test until the timepoint $t$; $M_t$ is the mass of drug released at the timepoint $t$, $DLC_{2mg}$ is the total mass of

drug contained in 2 mg of NiFe@C-PF127 MMCSNPs before the drug release test, and it is calculated starting from the drug loading content value and the amount of MMCSNPs employed (2 mg).

To determine if the differences between the three CDR average values belonging to the three release systems for each time point were statistically significant, the ANOVA statistical test was applied, setting the confidence level at 95%. To find out the equations that best describe the kinetics of drug release, mathematical modeling based on a non-linear regression approach was performed, taking into consideration six models: zero-order, first-order, Higuchi, Hixon-Crowell, Korsmeyer-Peppas and Weibull model (

Table 1). Each model describes a function that correlates the amount of drug released (dependent variable) with time (independent variable) through parameters and constants. For each mathematical model, the best curve fitting the experimental data was determined by using a non-linear Generalized Reduced Gradient (GRG) algorithm by numerical minimization of the sum of squared residuals [45]. Then, the models were evaluated by comparing the adjusted correlation coefficient ($R^2$) between the fitting and the experimental release curves. Furthermore, parity plots were used to compare the experimental DCR with the values predicted by the models at different times.

## 3. Results and discussion

### 3.1. Characterization of fresh MMCSNPs

The physicochemical analysis of NiFe@C-PF127 is crucial to determine if it can be applied as a nanocarrier for drug delivery. For this reason, an exhaustive characterization of the MMCSNPs was performed in this work to study the architecture, size, chemical composition, colloidal stability, porosity and magnetic properties of the developed MMCSNPs.
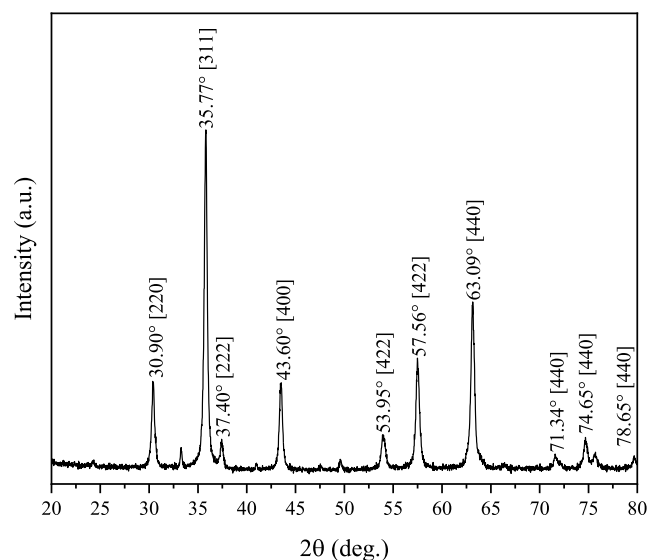
#### 3.1.1. Crystal phase of NiFe

To confirm the achievement of the nickel ferrite structure, NiFe core samples were analyzed by XRD, as shown in Fig. 2. The inverse spinel and face-centered cubic structure of nickel ferrite crystal was confirmed using the $NiFe_2O_4$ reference card 96-591-0065 from Crystallography Open Database (COD). Other studies in the literature also found similar diffractograms for nickel ferrite cores [46,47]. Starting from these data, the average crystal size was calculated applying four mathematical



**Fig. 2.** X-ray difractogram of the NiFe sample synthesized by sol/gel method and thermal treated at up to 1000 °C. 36.

approaches: Scherrer, Halder-Wagner, Williamson-Hall and Size Strain Plot methods, as described by *Nath* et al. [42]. Table S1 lists the equation employed for each technique. The core sizes obtained by these methods are 25.3, 12.6, 22.4 and 22.7 nm by Scherrer's equation, Halder-Wagner's, Williamson – Hall's and Size-Strain methods, respectively. These values were smaller than those reported in recent literature [48, 49], supporting the efficacy of the synthesis protocol for synthesizing nickel ferrite nanoparticles with desired crystallite size.

#### 3.1.2. Morphology

The particle size of NiFe and NiFe@C MMCSNPs was roughly estimated by analyzing the TEM images with ImageJ software.

This analysis revealed that NiFe and NiFe@C MMCSNPs have an average diameter of 13.62 ± 0.47 nm for the bare core (Fig. 3a), and 25.09 ± 0.58 nm for NiFe@C-PF127 (Fig. 3b). The histograms obtained for both samples are shown in Fig. 3c (NiFe) and Fig. 3d (NiFe@C-PF127). The crystallite size found for NiFe using the mathematical methods revealed that Halder-Wagner was the best mathematical model, reaching 7% error. It is important to highlight that comparison of MMCSNPs size observed in TEM images with the crystallite size found with mathematical models applied to XRD patterns is valid because nanoparticles are comprised of single crystallites, as can be seen in the images. Fig. 3b illustrates a magnified TEM image of NiFe@C MMCSNPs that confirms the multi-core shell structure. The images revealed a thin dark gray layer (the carbon shell) containing a more electron-dense zone (the core). Other similar methodologies dealing with the synthesis of magnetic nanoparticles for biomedical applications by the modified Stöber method have reported final nanoparticles' size of 150 nm [50], significantly higher than the value found in this study. In previous work using a similar carbon-coating procedure, the final nanoparticles achieved around 17 nm size [22]. However, in that case, the multi-core structure comprised magnetite cores smaller than the nickel ferrite ones used in this study. It is important to highlight that using magnetite as a magnetic core can result in loss of magnetic activity over time due to the partial oxidation of the core to maghemite, which is disadvantageous in this case. A study reported in the literature evaluated the impacts on surface and crystal properties of magnetite after oxidation, demonstrating that oxidation is catalyzed under acidic conditions [51]. Considering the target biomedical application in which the nanoparticle will go through acid environments (*i.e.*, tumor environment and endosome/lysosome microenvironment), this could represent complications

**Table 1**
Mathematical models involved in kinetic modeling of drug release.

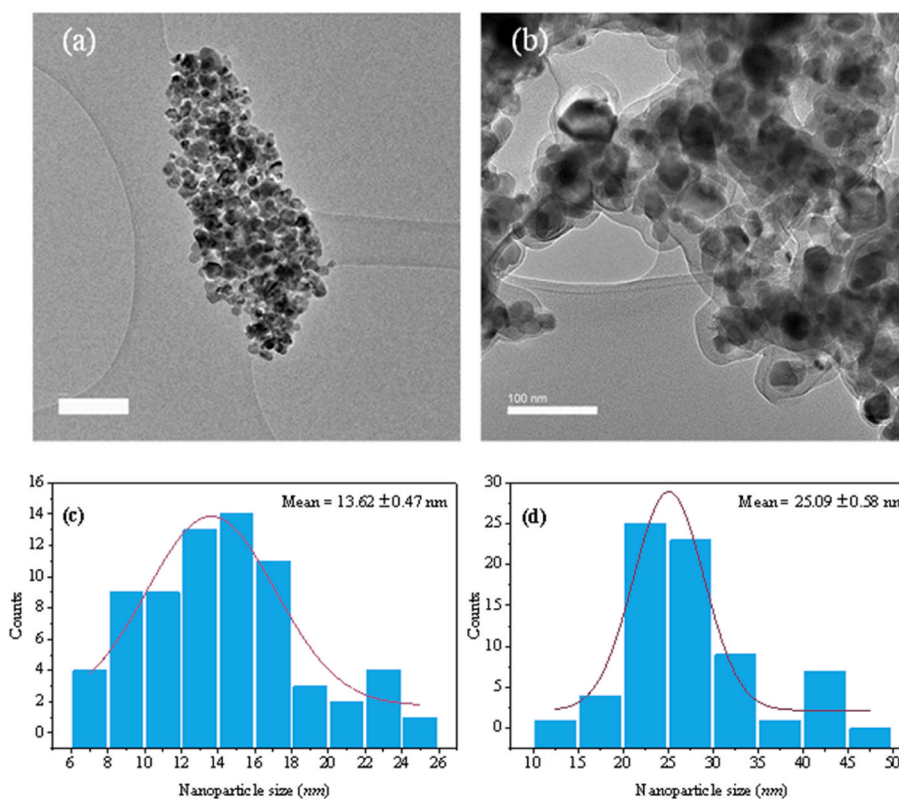| | Equation | Parameters and Variables |
|---|---|---|
| Zero-order | $M_t = k_0 \times t + M_0$ | $M_t$: mass of drug released at the timepoint t (µg); $k_0$: zero-order constant; t: timepoint (hours); $M_0$: initial mass of drug released (Mo = 0 µg). |
| First-Order | $ln\ C_t = ln\ C_0 - \dfrac{k \times t}{2.303}$ | $C_t$: remaining concentration of drug in nps at timepoint t; $C_0$: Initial concentration of drug in nps; t: timepoint (hours); k: first-order constant. |
| Higuchi | $f_t = k_H \times \sqrt{t}$ | $f_r$ = fraction of drug released; $k_h$ = Constant of Higuchi. |
| Korsmeyer-Peppas | $f_t = k \times t^n$ | k: constant of incorporation; t: timepoint (hour); n: exponent of release. |
| Hixon-Crowell | $\sqrt[3]{M_t} = \sqrt[3]{M_0} - k \times t$ | $M_t$: mass of drug remaining in nps on time t (µg); $M_0$: initial mass of drug contained in nps (µg); k: constant of incorporation; t: timepoint (hour). |
| Weibull | $M_t = M_0 \times \left(1 - e^{-\dfrac{t^\beta}{\alpha}}\right)$ | $M_t$: mass of drug released on time t (µg); $M_0$: total amount of drug being released (µg); α: parameter describing the time dependence; β: parameter describing the shape of dissolution curve. |

**Fig. 3.** TEM images of (a) NiFe and (b) NiFe@C-PF127 MMCSNPs. Nanoparticles size distribution calculated with ImageJ for (c) NiFe and (d) NiFe@C-PF127. 37.

during the therapy.

For biomedical purposes, smaller nanoparticles are desired to increase nanoparticle circulation in the blood network for a sustained period. Previous studies reported in the literature suggest that nanoparticles' sizes should not be above 100 nm to reach tumor tissues by passing through vascular structures. On the other hand, another author suggested that the size range 20–200 nm, which is more intermediate, has the highest potential for *in vivo* applications. Nevertheless, the size found for the nanoparticles used in this study is in the range recommended in the literature [52].

### 3.1.3. Surface characteristics

Surface characteristics of the selected materials were assessed by FT-IR. The analysis of the samples through the synthesis process revealed the presence/absence of specific key compounds, giving a hint regarding the successful synthesis procedure. The results obtained for the analysis are shown in Fig. 4 for all samples. All spectra showed peaks at 488, 600 and 809 cm$^{-1}$, which are ascribed to the typical vibration of the metal ions in the nickel ferrite crystal lattice of the core. The most relevant information retrieved from this analysis is the presence of Si–O, Si–O–Si, and Si–C bonds in the coated nanoparticle, confirmed by bands in 471, 796, 960, 1092, and 1235 cm$^{-1}$, respectively. The absence of these bands for samples obtained in the subsequent steps, NiFe@C, NiFe@C-ox, and NiFe@C-PF127, confirm the removal of the silica during the etching procedure. In this sense, this technique allows corroborating that multi-core shell nanoparticles are formed by removing silica previously present in the interstitial spaces between the cores. The sample obtained after oxidation with nitric acid did not reveal any alteration compared to the NiFe@C sample. Peaks at 1110 and 2800 cm$^{-1}$ emerged for the functionalized sample, NiFe@C-PF127, related to the presence of Pluronic® F-127 alkyl chains due to surface functionalization. Previous studies dealing with surface functionalization already detected the presence of alkyl chains due to functionalization [32] and the absence of silica groups in nanoparticles after etching [22]. However, to the best of
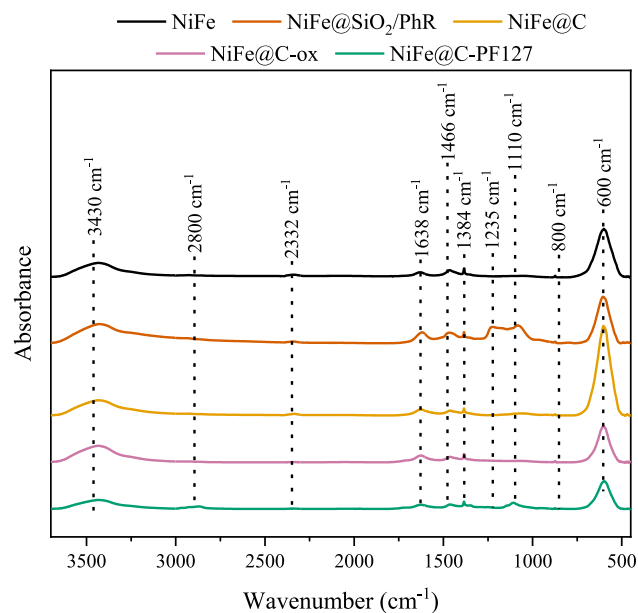


**Fig. 4.** FT-IR spectra of NiFe@SiO$_2$/C nanoparticles and NiFe@C-PF127 MMCSNPs. 38.

our knowledge, no other works report step-by-step characterization.

### 3.1.4. Thermal stability

Studies dealing with the biomedical application of nanoparticles based on nickel ferrite often do not report the thermogravimetric analysis of the magnetic nanoparticle, representing a gap in the literature [53–55]. In this study, thermogravimetric analysis (TGA) was carried

out for selected samples to evaluate thermal stability and obtain the differential thermogravimetric (DTG) by the first derivative of mass loss (wt.%) over time to find peaks related to mass loss of specific groups. The results obtained for TGA of samples NiFe, NiFe@SiO$_2$/PhR, NiFe@SiO$_2$/C, and NiFe@C are shown in Fig. 5a. The lowest mass loss (wt.%) was obtained for the nickel ferrite sample, reaching around 0.11 wt% at the end of the analysis. The high inorganic content confirmed by this result demonstrates the ability of the sol-gel methodology used in this work to prepare iron-based nanoparticles without organic contamination. In contrast, other studies dealing with nickel ferrite have reported values in the range of 8–60 wt% mass loss using sol-gel combustion to prepare nickel ferrite nanoparticles [56–58]. Among the developed nanoparticles of this work, the highest mass loss is observed for the NiFe@SiO$_2$/PhR sample, consistent with previous results obtained in another work using a similar resin for carbon coating of magnetic nanoparticles [22] and ascribed to the thermal decomposition of the organic phenolic resin. The difference in mass loss observed for NiFe@SiO$_2$/C and NiFe@C demonstrates that small quantities of organic matter are removed during etching with NaOH, *i.e.*, the etching process is a selective treatment efficient for the removal of silica.

The results obtained for DTG are illustrated in Fig. 5b. The peak observed in the range 80–120 °C is related to removing adsorbed water from the nanomaterials and it was presented for all samples. The peaks in the range of 200–550 °C obtained for the coated sample are related to the decomposition of OH groups from silanols and the oxidation of the polymeric resin. The absence of peaks around 200 °C for the sample obtained after etching is another hint regarding the successful removal of silica from the nanoparticles, indicating the formation of the desired nanoparticle's architecture. Apart from the core, all samples have peaks in the range of 400–550 °C, ascribed to the oxidation of the carbon content from the nanoparticles.
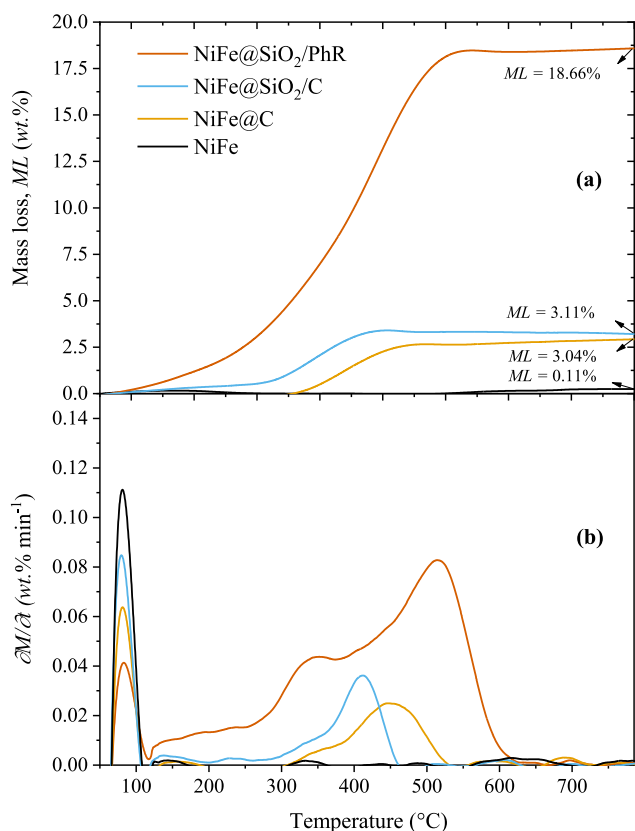
### 3.1.5. Composition

Table 2 summarizes the CHNS-elemental composition of NiFe@-SiO$_2$/PhR and NiFe@SiO$_2$/C MMCSNPs. The carbon content of NiFe@-SiO$_2$/C (2.17 wt%) agrees with the results reported for TGA analysis. Furthermore, as observed, after annealing, MMCSNPs underwent a consistent mass loss. In detail, carbon and hydrogen weight decreased by 78.5 and 97.2 wt%, while nitrogen was completely removed. The knowledge of the synthesis procedure suggests that carbon and hydrogen result from the condensation reaction of TEOS and the polymerization reaction of resorcinol and formaldehyde, the main reactions involved in polymeric resin formation. Nitrogen content in coated nanoparticles comes from byproducts of coating reaction involving the utilization of ammonia. The high increase in the C/H ratio observed for the sample recovered after thermal treatment is explained by the carbonization process, in which dehydration and aromatization reactions occur [59,60]. To the best of our knowledge, carbon-based nanoparticles reported in the literature for biomedical applications are not characterized by CHNS elemental analysis, so the results found here cannot be compared to the literature [22,31,61]. In fact, the carbon content found for the final sample and the increased C/H ratio are fundamental to confirm that the resin is carbonized in the annealing process and not completely degraded by the temperature. The remaining content (R) of the samples can be ascribed to the presence of oxygen in the materials. As NiFe@SiO$_2$/PhR has an organic resin, thus containing phenolic groups, it is expected that NiFe@SiO$_2$/PhR has more oxygen than NiFe@SiO$_2$/C. As inorganic matter (I.M.) in samples was determined as the residual matter obtained in samples by TGA in air atmosphere, oxygen linked to metal framework is counted in I.M., thus, the remaining content (R) present in Table 2 only refers to the oxygen presence in the organic matrix.

### 3.1.6. Magnetic properties

Magnetic drug targeting is usually performed upon applying an external magnetic field from a permanent magnet or electromagnetic coils [62]. Another alternative would be using stationary magnetic fields to attract the magnetic drug nanocarriers [63]. Studies were already reported in the literature to evaluate diverse aspects of both approaches, to search for advantages and difficulties, and seek information to increase the applicability of iron oxide nanoparticles in real theranostics [5]. Nonetheless, developing suitable nanocarriers with biocompatibility, proper size, stability in water, and sufficient magnetic properties remains a challenge. For this reason, one important parameter to be evaluated when developing new nanocarriers is their magnetic properties. In this regard, previous studies have reported primary issues related to utilizing superparamagnetic nanocarriers comprised of single nanoparticles because they do not display high magnetization [64]. One strategy to overcome this problem is the synthesis of clustered nanoparticles to increase their overall magnetic response or avoid the loss of magnetic activity due to surface modification treatments. In this study,



**Fig. 5.** (a) TGA and (b) DTG results for NiFe, NiFe@SiO$_2$/C, NiFe@/C and NiFe@SiO$_2$/PhR samples under oxidant conditions. 39.

**Table 2**
Composition of samples before and after annealing of the coated sample with phenolic resin coupled with inorganic matter (I.M.) determined from results obtained by TGA in air atmosphere.

| Sample | C/H | C (wt. %) | H (wt. %) | N (wt. %) | S (wt. %) | I.M.[a] (wt.%) | R[b] (wt. %) |
|---|---|---|---|---|---|---|---|
| NiFe@SiO$_2$/ PhR | 9.7 | 10.1 ± 0.1 | 1.04 ± 0.03 | 1.32 ± 0.03 | 0.00 ± 0.00 | 81.34 | 6.20 |
| NiFe@SiO$_2$/ C | 67.8 | 2.17 ± 0.07 | 0.03 ± 0.01 | 0.00 ± 0.00 | 0.00 ± 0.00 | 97.00 | 0.79 |

[a] Determined by TGA.
[b] R is the remaining non identified composition by the techniques, determined as R = 100 – C – H – N – S – I.M.

magnetic characterization was performed for the bare nickel ferrite sample and final MMCSNPs to demonstrate that carbon-coating and surface functionalization do not significantly change the magnetic properties of the nanoparticles. In Fig. 6, the results of the magnetic analysis of NiFe cores and NiFe@C-PF127 MMCSNPs recorded at 300 K are described in terms of mass-relative magnetization (M) as a function of the applied magnetic field (H). In detail, NiFe cores and NiFe@C-PF127 MMCSNPs exhibit similar saturation magnetization $\sim$43 A $m^2$ $Kg^{-1}$, whereas the coercivity is 93 Oe and 69 Oe, respectively. For remnant magnetization, NiFe shows 1.8 A $m^2$ $Kg^{-1}$, and NiFe@C-PF127 shows 4.5 A $m^2$ $Kg^{-1}$. Low values of remnant magnetization and coercivity and high saturation magnetization observed for both samples agreed with those found in the literature for superparamagnetic nanoparticles [22,31]. Comparing the magnetic behavior of the initial sample (NiFe) with that of the final functionalized nanoparticle (NiFe@C-PF127) reveals no significant alteration, demonstrating that the magnetic response loss expected due to carbon coating is compensated by the multi-core shell architecture. In other words, the saturation magnetization remained the same due to the final multi-core structure, increasing the magnetic response of the nanocarrier. Nonetheless, the low reduction in coercivity, remanent and saturation magnetization can be attributed to the lower dipolar interaction between the cores due to the presence of carbon-based shell on final nanoparticles.

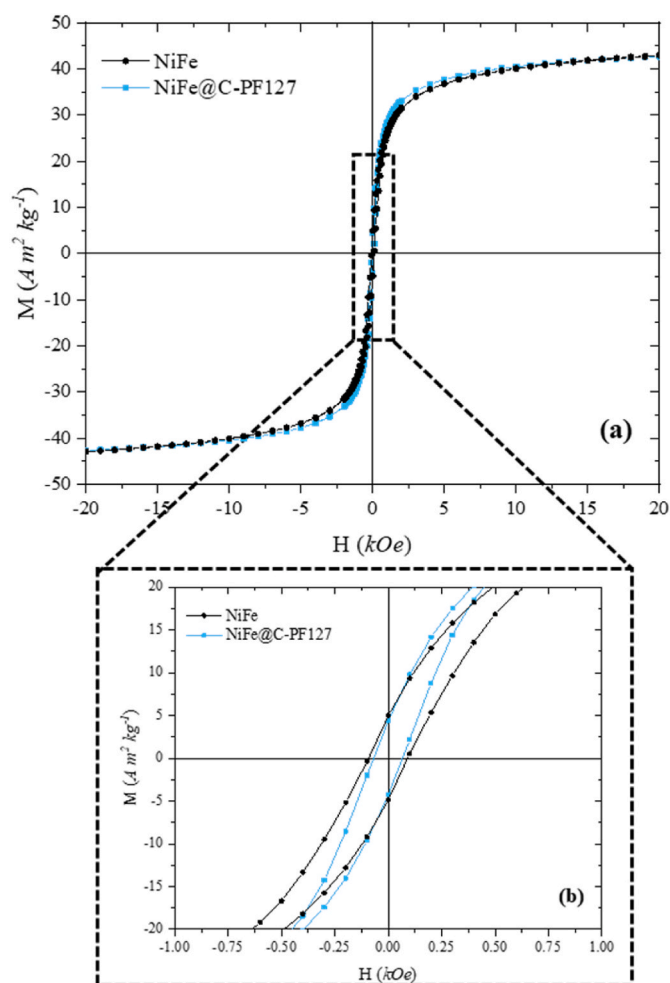For instance, other studies dealing with synthesizing superparamagnetic nanoparticles for biomedical applications have reported higher saturation magnetization values [31,33,61]. On the other hand, most studies reporting higher values considered the utilization of magnetite as the core in their approach, but the authors did not address the magnetic activity loss due to the partial oxidation of the magnetic core. Some other studies are reporting smaller values for saturation magnetization, such as the work performed by Ao et al. (32.5 A $m^2$ $kg^{-1}$) [65]. Nonetheless, another study reported in the literature that the external magnetic field could not be used to guide nanoparticles during an essay performed if the saturation magnetization was lower than 30 A $m^2$ $kg^{-1}$ [66]. For this reason, the magnetic characterization of NiFe@C-PF127 indicates that the material is suitable for MDT applications since superparamagnetism was confirmed, with a saturation magnetization value higher than 30 A $m^2$ $kg^{-1}$.

### 3.1.7. Textural properties: specific surface area and pore volume

NiFe@C and NiFe@SiO$_2$/C MMCSNPs were analyzed by N$_2$ adsorption/desorption, according to the Brunauer–Emmett–Teller (BET) theory, to determine the surface areas of the as-synthesized magnetic nanoparticles. The analysis of these samples allows an understanding of the etching effect on the nanoparticles, for which an increase in surface area is expected, resultant from the removal of silica and the formation of pores in carbon shell and interstitial space in the multi-core structure. The obtained adsorption and desorption curves are reported in Fig. S1, and they exhibit an intermediate shape between the isotherm category IV and V with an H4-type hysteresis loop. As the overall isotherm shape indicates the mesoporous nature of NiFe@C MMCSNPs, the parallel branches of the H4 hysteresis loop in the relative pressure between 0.18 and 1.0 are attributable to the interstitial space between the cores [67, 68]. The BET specific surface area ($S_{BET}$), the total pore volume ($V_{mic}$), and the average pore width values of NiFe@C cores and NiFe@SiO$_2$ MMCSNPs are compared in Table 3. As observed, NiFe@C MMCSNPs have an average pore width of 2.2 nm in agreement with the mesoporous range, a $S_{BET}$ of 38 $m^2$ $g^{-1}$, and a $V_{mic}$ of 6 $mm^3$ $g^{-1}$. These values indicate that, as desired, the mesoporous carbon shell increased the surface area and the pore volume since they are respectively two and six times higher than the value of the NiFe@SiO$_2$/C sample. Even though some works dealing with the biomedical application of carbon-based magnetic nanoparticles refer to the importance of the high surface area but do not present the characterization for their nanoparticles [31], the analysis of textural properties from resorcinol/formaldehyde coated nanoparticles is not frequently detailed on the literature [69]. Furthermore, even for studies reporting the surface area of their nanoparticles, there is no discussion regarding the hysteresis type, pore width and micropore volume [33,61], especially evaluating the textural properties of the nanoparticles in different steps of the synthesis.

### 3.1.8. DLS and zeta potential

DLS result for NiFe@C-PF127 showing nanoparticles size distribution is illustrated in Fig. 7. The fact that functionalized MMCSNPs present enough stability in water to carry out the analysis demonstrates the high stability of the MMCSNPs. Considering the application for which the MMCSNPs were designed, colloidal stability in water is an important characteristic to avoid aggregation and increase blood circulation time [70]. The average hydrodynamic diameter calculated based on the result for NiFe@C-PF127 was 167 $\pm$ 59.4 nm, with a polydispersion



**Fig. 6.** (a) Magnetization curves of NiFe core and NiFe@C-PF127 MMCSNPs (H: applied magnetic field, M: mass-relative magnetization); (b) zoomed region around origin point. 40.

**Table 3**
Textural properties of samples before (NiFe@SiO$_2$/C) and after (NiFe@C) etching.

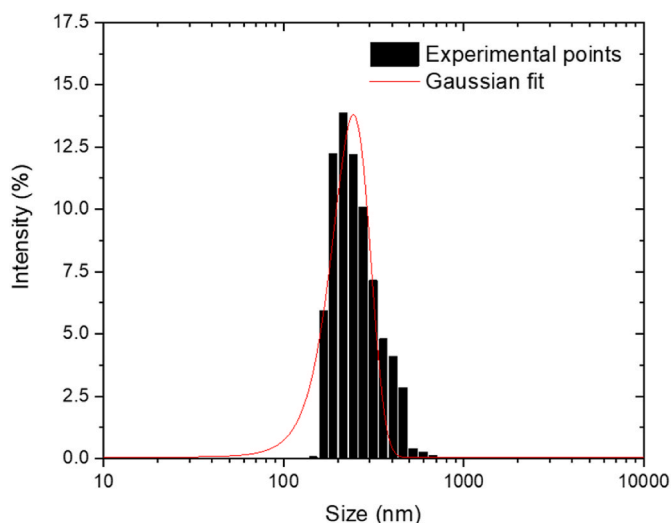| | $S_{BET}$ ($m^2$ $g^{-1}$) | $S_{ext}$ ($m^2$ $g^{-1}$) | $S_{mic}$ ($m^2$ $g^{-1}$) | $V_{mic}$ ($mm^3$ $g^{-1}$) | $V_{Total}$ ($mm^3$ $g^{-1}$) | $W_{mic}$ (nm) |
|---|---|---|---|---|---|---|
| NiFe@SiO$_2$/C | 19 | 17 | 2 | 1 | 57 | 2.0 |
| NiFe@C | 38 | 27 | 11 | 6 | 79 | 2.2 |

**Fig. 7.** Dynamic light scattering of NiFe@C-PF127. X-axys (size) represented in logarithmic scale. 41.

index (PDI) of 0.12. According to the literature, nanoparticles ranging from 10 to 200 nm are more likely to accumulate in the tumor than in healthy tissues due to the enhanced permeability and retention (EPR) effect [71]. Furthermore, particles with hydrodynamic diameter in the range of 100–200 nm are large enough to avoid retention by the liver and splenic filtration [61]. The zeta potential of final nanoparticles is also important to measure the affinity of the functionalized MMCSNPs with drugs. According to measurements, the zeta potential of the NiFe@C-PF127 is $-56.8$ mV, which is higher than the values reported in other works using the same functionalization of carbon-coated magnetic nanoparticles [31,61]. The strong negative charge found for the functionalized nanoparticles is a direct consequence of PF-127 functionalization, as already reported in a previous work [32]. Another advantage coming from negatively charged nanoparticles is increased blood circulation due to the ability to avoid opsonization phenomenon, which is responsible for elimination of bodies by macrophage cells [32]. Moreover, the negatively charged surface of nanoparticles is fundamental for the loading of cationic drugs, as those considered in this study. Therefore, NiFe@C-PF127 has an optimal dimension for application as drug nanocarriers via intravenous administration.

### 3.2. Core stability

Fig. S2 shows the iron and nickel leaching observed for bare core (NiFe sample) when nickel ferrite nanoparticles were used in the different mediums studied (PBS at pH 4.5, 6.0 and 7.4). According to the metal quantification results, it is possible to observe a strict correlation between iron and nickel leached from the bare core with the pH. In this case, acidic pH correlates with higher metal leaching from the bare core nanoparticles, which agrees with data in the literature [33]. The amount of iron and nickel released by the core corresponds to 3.66, 2.64 and 1.84% of mass loss for iron and 3.46, 2.29 and 1.3% for nickel in PBS at pH 4.5, 6.0 and 7.4. On the other hand, the amounts of iron and nickel released by the functionalized nanoparticles were negligible and inferior to the detection limit of the equipment used, evidencing the successful development of the carbon shell structure of this study. The results indicate that NiFe@C-PF127 would not face issues in real applications regarding the release of undesired components in patients.

### 3.3. Drug loading

To investigate the possible application of NiFe@C-PF127 as drug nanocarriers, the MMCSNPs were separately loaded with DOX and OME,

and assessed through DLC and DLE determination. Impressively, it was found that 481.8 µg of DOX are loaded per mg of NiFe@C-PF127, achieving a DLE value as high as 96.68%. Regarding OME, the DLE of NiFe@C-PF127 reaches 51.35%, reaching a DLC of 153.4 µg mg$^{-1}$. Overall, such results confirm the extraordinary capacity of NiFe@C-PF127 to accumulate a large amount of pharmacological compounds. For instance, previous works with a similar design for drug loading assays achieved 91% [32] and 93.6% [22] DLE for DOX. To the best of our knowledge, there are no studies in the literature dealing with OME loading for theranostic purposes, as proposed in this present study.

FT-IR of drug loaded nanoparticles is important to determine if the DLC and DLE results are valid since the methodology used to evaluate the drug loading performance considers drug concentration in liquid media. In this regard, the evaluation performance could be misleading if the drug precipitated during the procedure and is not loaded into the nanocarrier (either on its surface or its interior). FT-IR results for pure drugs and loaded NiFe@C-PF127 are shown in Fig. S3. The result obtained for pure drugs revealed high similarity with reported literature [72,73]. Comparing the functionalized nanoparticles spectra with the result obtained for both drug loaded nanoparticles reveals different results, which are related to the presence of the drug on the nanoparticles. For instance, DOX loaded nanoparticles exhibited bands at 1608, 1573, 1285, and 805 cm$^{-1}$ that are ascribed to the presence of the medicine loaded in the nanocarrier. The same result was obtained for OME loaded NiFe@C-PF127, with the bands at 3060, 1408, and 822 cm$^{-1}$ confirming the successful loading of the medicine in the nanoparticle. The identification of bands ascribed to the presence of drugs in the samples represents a qualitative confirmation of the results obtained for loading performance since the drug is indeed being loaded during loading experiments.

UV–Vis spectra of aliquots before and after the loading procedure performed without MMCSNPs (*i.e.* 0.5 and 0.3 mg mL$^{-1}$ DOX and OME solutions, respectively, were stirred inside an orbital shaker at room temperature for 48 h, subjected to centrifugation, frozen and lyophilized overnight at 0.04 mbar and $-46\,^\circ$C) confirmed that the loading protocol considered in this study is not resulting drugs degradation since UV–Vis spectra were the same for both samples in each run.

### 3.4. Drug release

Cancer cells produce a peculiar microenvironment characterized by abnormal biochemical properties compared to normal tissue. High acidity, hypoxia and altered redox equilibrium are some of the most common changes observed in solid tumors that support the survival of the cancer cells inside the body. Nanotechnology can use these features to develop smart nanocarriers that release the drug in response to a specific tumor environmental stimulus [29]. In this perspective, MMCSNPs were designed to adsorb drugs and trigger the release of the medicaments as a consequence of the peculiar tumor acidity. To assay such pH-sensibility, MMCSNPs loaded with DOX (NiFe@C-PF127-Dox) and OME (NiFe@C-PF127-Ome) underwent release tests conducted in three levels of acidity: 7.4, 6.0 and 4.5, mimicking the physiological condition, the tumor microenvironment and the endosome pH, respectively. Fig. 8A illustrates the results of the DOX release tests in cumulative drug release (CDR) over time. A pH-dependent release profile of the drug is easily noticeable as MMCSNPs release a higher amount of DOX in progressively more acid environments. In detail, after an incubation of 48 h, the total amount of DOX released was 20.0%, 15.9% and 13.1% for PBS at pH 4.5, 6.0 and 7.4, respectively. The cause of this behavior lies in the fact that acidity determines the protonation of nanoparticle anionic surface groups, thereby disrupting the electrostatic interactions between the MMCSNPs and the cationic drug. Concerning the OME drug release, the results are illustrated in Fig. 8B. For this case, verifying a pH-dependent drug release was also possible. However, as the major fraction of release occurred at pH 4.5 (CDR = 70.0%), MMCSNPs liberated more OME at pH 7.4 (CDR = 61.5%) than at 6.0
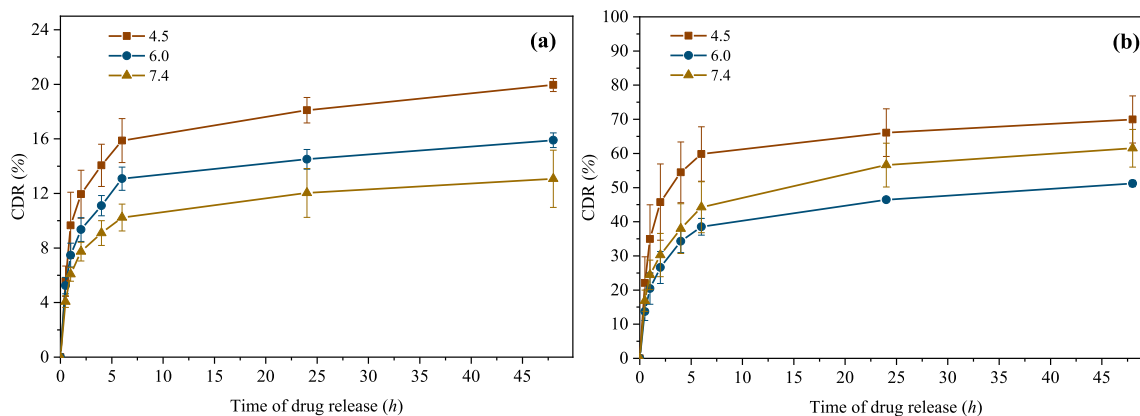
**Fig. 8.** pH-dependent release kinetics of (a) doxorubicin and (b) omeprazole in terms of percentage cumulative drug release (CDR) in function of time. 42.

(CDR = 51.2%). Such behavior is due to the OME chemical structure that becomes negatively charged at pH values higher than 7.1, like the particle surface [74]. Therefore, when NiFe@C-PF127-Ome MMCSNPs are suspended in a PBS buffer at pH 7.4, the repulsive forces between the same negatively charged surface particle and molecules promote the release of the drug. The higher release percentage of OME compared to DOX observed for this study is related to the electrostatic bond strength of loaded drugs with NiFe@C-PF127. In this regard, DOX has a higher electrostatic interaction with NiFe@C-PF127 than OME, which explains the higher release of OME for the tests performed [75,76].

Previous studies dealing with DOX delivery using carbon-based magnetic nanoparticles reached release values of 19, 52, and 75% in acidic pH [31,33,61]. These studies used a similar synthesis procedure as the one considered in this work. Still, they lacked characterization and did not evaluate their nanoparticles' loading mechanism, assuming the loading was successful in all cases. Other studies also reported delivery values up to 70% in acidic environments using chitosan-coated magnetic nanoparticles [77–80]. The lowest DOX release obtained in this work can be associated with the strong electrostatic interactions between nanoparticle and drug. For instance, the zeta potential of NiFe@C-PF127 (−56.3 mV) is significantly lower than in other works (−16.3 mV [78] and −37 mV [32]), reason why other works achieved higher DOX release percentages. Nevertheless, the authors did not show a detailed characterization of their nanoparticle or even determine the amount of iron leached due to exposure to an acidic medium. On top of the literature gaps briefly addressed here, the studies reported so far do not evaluate the capacity of their nanocarrier to load and release other anti-cancer drugs, such as OME.

ANOVA test was carried out for the released amount of DOX and OME at different times, and the result is illustrated in Fig. S4. The analysis of the *p*-value obtained for each time shows that after 2 h of the experiment the amount of DOX released is statistically different at different pH values. On the other hand, for OME, statistically different drug release was observed only after 4 h of the experiment. Nonetheless,

the controlled release of medicine according to the pH of the environment was proved for both medicaments by these means.

### 3.5. Kinetics of release

The kinetic results acquired from non-linear regression are listed in Table 4. They indicate that the release of DOX and OME is not properly described by zero and first-order models. On the contrary, non-linear equations coming from Korsmeyer-Peppas and Weibull models better fit the release profiles, as proven by the highest values of the correlation coefficient, reaching almost 0.9. The drug release profile obtained using both models is represented in Fig. 9. A parity plot for all models was made to compare the performance of the best models with the others studied, and the result is shown in Fig. S5 (best models) and Fig. S6 for the other models. Moreover, by analyzing the Korsmeyer-Peppas' release exponent and Weibull's beta parameter, it is possible to understand how the release rate changes over time and the mechanism driving the release.

As the Weibull's beta parameter is lower than the unit, from a mathematical point of view, each release curve outlines a parabolic arc, meaning the release rate is not constant over time as shown in Figure S6a (DOX) and Figure S6c (OME). Still, it decreases quickly throughout the first 5 h and then slowly as shown in Figure S6b (DOX) and Figure S6d (OME). Concerning the mechanism of release, as the Korsmeyer-Peppas coefficients are lower than 0.5, it is possible to hypothesize that the drug release is governed by Fickian diffusion [81]. In other words, DOX and OME diffuse from the nanoparticles' pores and act as a drug reservoir. Other study reported on the literature arrived at the same conclusion regarding non-linear models fitting better drug release profiles using carbon-coated nanoparticles functionalized with Pluronic ® F-127 [22]. A similar result obtained using different nanoparticles demonstrates that the superparamagnetic core does not significantly influence the nanoparticle's drug loading and release capacity. The comparison with other studies dealing with the kinetic modeling of DOX is complicated due to

**Table 4**

Constants, parameters and the adjusted coefficients of determination ($R^2$) obtained from the kinetic modeling of doxorubicin and omeprazole release studies.

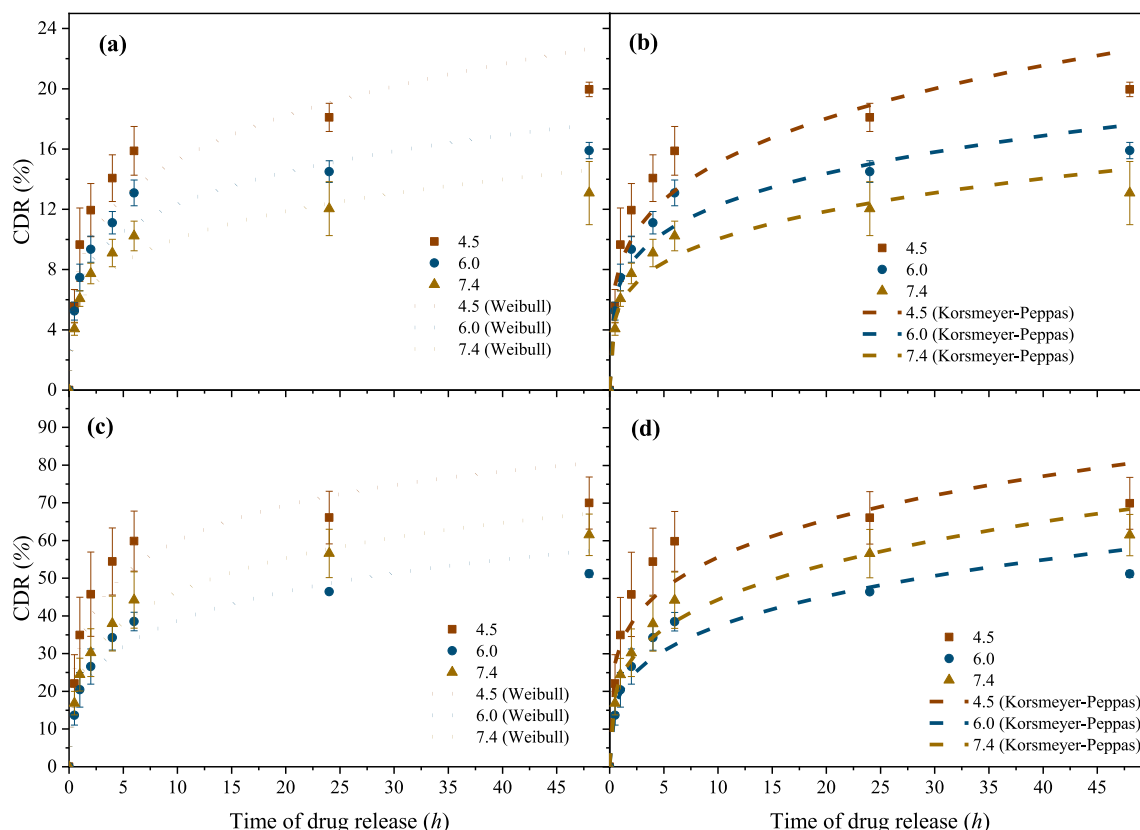| | DOXORUBICIN | | | | | | | | | | | | | | |
|---|---|---|---|---|---|---|---|---|---|---|---|---|---|---|---|
| | Zero-Order | | First-Order | | Higuchi | | Korsmeyer - Peppas | | | Hixon - Crowell | | Weibull | | |
| pH | $k_0$ ($h^{-1}$) | $R^2$ | $k$ ($h^{-1}$) | $R^2$ | $k_h$ ($h^{-0.5}$) | $R^2$ | $k_{KP}$ ($h^{-n}$) | $n$ | $R^2$ | $K$ ($h^{-1}$) | $R^2$ | $\alpha$ (h) | $\beta$ | $R^2$ |
| 4.5 | 0.0060 | 0.535 | 0.0136 | 0.562 | 0.0453 | 0.736 | 0.0835 | 0.257 | 0.849 | 0.0163 | 0.626 | 11.47 | 0.279 | 0.857 |
| 6.0 | 0.0048 | 0.553 | 0.0106 | 0.571 | 0.0363 | 0.757 | 0.0720 | 0.231 | 0.878 | 0.0130 | 0.572 | 13.38 | 0.246 | 0.884 |
| 7.4 | 0.0040 | 0.577 | 0.0086 | 0.593 | 0.0298 | 0.780 | 0.0573 | 0.243 | 0.893 | 0.0106 | 0.596 | 16.95 | 0.254 | 0.897 |
| **OMEPRAZOLE**rowhead | | | | | | | | | | | | | | |
| 4.5 | 0.021 | 0.429 | 0.072 | 0.572 | 0.162 | 0.647 | 0.323 | 0.236 | 0.790 | 0.0555 | 0.533 | 2.57 | 0.371 | 0.861 |
| 6.0 | 0.016 | 0.606 | 0.042 | 0.670 | 0.115 | 0.806 | 0.197 | 0.278 | 0.898 | 0.0352 | 0.671 | 4.58 | 0.351 | 0.925 |
| 7.4 | 0.019 | 0.673 | 0.056 | 0.772 | 0.138 | 0.861 | 0.235 | 0.276 | 0.940 | 0.0445 | 0.747 | 3.76 | 0.370 | 0.869 |

**Fig. 9.** (a–b) Omeprazol and (c–d) doxorubicin release profiles calculated with (a, c) Weibull model for and (b, d) Korsmeyer-Peppas. 43.

the lack of unities in the values reported by the authors and the vague description of how kinetic modeling was developed [39,82].

## 4. Conclusions

The presented work comes from the potential use of the MDT strategy to control the distribution of anticancer agents inside the body, carrying the medicament with magnetic nanoparticles and accumulating it specifically in the tumor site. To investigate such a delivery approach, in this paper, magnetic multi-core shell nanoparticles have been synthesized to load cationic drugs and release them in a tissue-specific way in response to the typical tumor acidity microenvironment. For this purpose, MMCSNPs have been prepared with a nickel ferrite magnetic core and a biocompatible porous carbon shell, following five synthesis steps: sol-gel synthesis of nickel ferrite cores, core-coating with silica and phenolic resin, carbonization, silica etching and shell functionalization.

The results obtained from the physicochemical characterization support achieving the final nanoproduct's desired features. NiFe@C-PF127 nanoparticles showed the multi-core shell architecture and a mesoporous carbon layer, as revealed by TEM images, BET analysis and $N_2$ adsorption/desorption isotherm curve. Moreover, the XRD diffraction pattern and SQUID analysis demonstrated the nickel ferrite nature of the cores and its superparamagnetic behavior. Furthermore, the extensive characterization reported here allows a better understanding of how each synthesis step influences the final architecture of the nanoparticles, permitting to better design the synthesis steps to reach the desired nanocarrier structure.

For biomedical purposes, the particle size, surface potential and composition play a crucial role because they determine the pharmacokinetics of MMCSNPs. The synthesis process guaranteed the preparation of a monodisperse product of multi-core shell nanoparticles with a

diameter of 25.09 nm, colloidally stable, and functionalized with the biocompatible polymer Pluronic® F-127, as indicated by the size distribution of hydrodynamic radius and the FT-IR spectrum.

The work's second part evaluated MMCSNPs ability as drug nanocarriers. Drug loading assays proved that NiFe@C-PF127 MMCSNPs could adsorb high amounts of DOX and OME, reaching a DOX loading efficiency of 97%. Moreover, the most striking result comes from release tests that confirmed the influence of acidity level on the drug release profile from the particles: the more acidic the environment, the higher the amount of the drug released. However, this behavior is partially true for the release of OME because nanoparticles unload more drug at pH 7.4 than 6.0 due to the repulsive forces between the negatively charged particle surface and the OME anionic form at pH value higher than 7.1. In future works, the functionalization could be modified to increase the zeta potential and decrease the electrostatic bond between nanoparticles and DOX, which can increase the amount of DOX delivered in tumorous environments.

Considering the aims of this work, it is possible to conclude that the synthesized magnetic nanoparticles not only have all the main chemical and physical features required for their application as delivery nanocarriers of anticancer drugs, but they also show a smart release of the loaded medicaments, related with the target microenvironment. In this regard, magnetic nanocarriers can become highly tissue-specific, leaning on an inside/outside double targeting system: the external magnetic pointing combined with the inner drug release triggered by the characteristic tumor acidity. Additionally, a kinetic study revealed the prevalence of non-linear models to fit the release rate, with the Fickian diffusion ruling mechanism in drug release from the nanocarrier. Future work should enhance the particle shell's porosity and evaluate the particles' biological characteristics through *in vitro* cell tests.

## Credit authorship contribution statement

Simone Moretto – Investigation, Visualization, Formal analysis, Writing – original draft. Adriano Santos Silva – Investigation, Visualization, Formal analysis, Validation, Writing – original draft, Methodology. Jose L. Diaz de Tuesta – Conceptualization, Validation, Writing – Review & Editing, Project administration. Fernanda F. Roman – Writing – Review & Editing. Rita Cortesi – Supervision. Ana Raquel Bertão – Investigation. Manuel Bañobre-López – Supervision. Marta Pedrosa – Investigation. Adrián M.T. Silva – Writing – Review & Editing, Supervision. Helder T. Gomes – Writing – Review & Editing, Supervision, Project administration, Funding acquisition.

## Declaration of competing interest

The authors declare that they have no known competing financial interests or personal relationships that could have appeared to influence the work reported in this paper.

## Data availability

No data was used for the research described in the article.

## Acknowledgments

## Appendix A. Supplementary data

Supplementary data to this article can be found online at https://doi.org/10.1016/j.mtchem.2023.101748.

## References

[1] K.S. Saini, C. Twelves, Determining lines of therapy in patients with solid cancers: a proposed new systematic and comprehensive framework, Br. J. Cancer (January, 2021), https://doi.org/10.1038/s41416-021-01319-8.

[2] S. Gul, S.B. Khan, I.U. Rehman, M.A. Khan, M.I. Khan, A comprehensive review of magnetic nanomaterials modern day theranostics, Front. Mater. 6 (2019) 1–15, https://doi.org/10.3389/fmats.2019.00179.

[3] N. Hoshyar, S. Gray, H. Han, G. Bao, The effect of nanoparticle size on in vivo pharmacokinetics and cellular interaction, Nanomedicine 11 (6) (2016) 673–692, https://doi.org/10.2217/nnm.16.5.

[4] S.M. Hosseini, J. Mohammadnejad, S. Salamat, Z. Beiram Zadeh, M. Tanhaei, S. Ramakrishna, Theranostic polymeric nanoparticles as a new approach in cancer therapy and diagnosis: a review, Mater. Today Chem. 29 (2023), 101400, https://doi.org/10.1016/j.mtchem.2023.101400.

[5] P.M. Price, W.E. Mahmoud, A.A. Al-Ghamdi, L.M. Bronstein, Magnetic drug delivery: where the field is going, Front. Chem. 6 (DEC) (2018) 1–7, https://doi.org/10.3389/fchem.2018.00619.

[6] P. Kheirkhah, et al., Magnetic drug targeting: a novel treatment for intramedullary spinal cord tumors, Sci. Rep. 8 (1) (2018) 1–9, https://doi.org/10.1038/s41598-018-29736-5.

[7] J. Zhu, J. Wang, Y. Li, Recent advances in magnetic nanocarriers for tumor treatment, Biomed. Pharmacother. 159 (December 2022) (2023), 114227, https://doi.org/10.1016/j.biopha.2023.114227.

[8] X. Li, W. Li, M. Wang, Z. Liao, Magnetic nanoparticles for cancer theranostics: advances and prospects, J. Contr. Release 335 (May) (2021) 437–448, https://doi.org/10.1016/j.jconrel.2021.05.042.

[9] N. Kritika, I. Roy, Therapeutic applications of magnetic nanoparticles: recent advances, Mater. Adv. 3 (20) (2022) 7425–7444, https://doi.org/10.1039/d2ma00444e.

[10] D.A. Alromi, S.Y. Madani, A. Seifalian, Emerging application of magnetic nanoparticles for diagnosis and treatment of cancer, Polymers 13 (23) (2021) 1–26, https://doi.org/10.3390/polym13234146.

[11] A. Farzin, S.A. Etesami, J. Quint, A. Memic, A. Tamayol, Magnetic nanoparticles in cancer therapy and diagnosis, Adv. Healthcare Mater. 9 (9) (2020) 1–57, https://doi.org/10.1002/adhm.201901058.

[12] L. García-Hevia, et al., Magnetic lipid nanovehicles synergize the controlled thermal release of chemotherapeutics with magnetic ablation while enabling non-invasive monitoring by MRI for melanoma theranostics, Bioact. Mater. 8 (May 2021) (2022) 153–164, https://doi.org/10.1016/j.bioactmat.2021.06.009.

[13] B.D. Cardoso, et al., Magnetoliposomes based on shape anisotropic calcium/magnesium ferrite nanoparticles as nanocarriers for doxorubicin, Pharmaceutics 13 (8) (2021), https://doi.org/10.3390/pharmaceutics13081248.

[14] M. Cerqueira, E. Belmonte-Reche, J. Gallo, F. Baltazar, M. Bañobre-López, Magnetic solid nanoparticles and their counterparts: recent advances towards cancer theranostics, Pharmaceutics 14 (3) (2022), https://doi.org/10.3390/pharmaceutics14030506.

[15] J. Jiménez-López, L. García-Hevia, C. Melguizo, J. Prados, M. Bañobre-López, J. Gallo, Evaluation of novel doxorubicin-loaded magnetic wax nanocomposite vehicles as cancer combinatorial therapy agents, Pharmaceutics 12 (7) (2020) 1–16, https://doi.org/10.3390/pharmaceutics12070637.

[16] Y.S. Ong, M. Bañobre-López, S.A. Costa Lima, S. Reis, A multifunctional nanomedicine platform for co-delivery of methotrexate and mild hyperthermia towards breast cancer therapy, Mater. Sci. Eng. C 116 (2020), https://doi.org/10.1016/j.msec.2020.111255.

[17] M. Priebe, K.M. Fromm, Nanorattles or yolk-shell nanoparticles-what are they, how are they made, and what are they good for? Chem. Eur J. 21 (10) (2014) 3854–3874, https://doi.org/10.1002/chem.201405285.

[18] X. Chen, et al., Optical and magnetic properties of small-size core–shell Fe3O4@C nanoparticles, Mater. Today Chem. 22 (2021), 100556, https://doi.org/10.1016/j.mtchem.2021.100556.

[19] A.G. Díez, M. Rincón-Iglesias, S. Lanceros-Méndez, J. Reguera, E. Lizundia, Multicomponent magnetic nanoparticle engineering: the role of structure-property relationship in advanced applications, Mater. Today Chem. 26 (2022), https://doi.org/10.1016/j.mtchem.2022.101220.

[20] S.E. Sandler, B. Fellows, O. Thompson Mefford, Best practices for characterization of magnetic nanoparticles for biomedical applications, Anal. Chem. 91 (22) (2019) 14159–14169, https://doi.org/10.1021/acs.analchem.9b03518.

[21] A. Akbarzadeh, M. Samiei, S. Davaran, Magnetic nanoparticles: preparation, physical properties, and applications in biomedicine, Nanoscale Res. Lett. 7 (1) (2012) 144, https://doi.org/10.1186/1556-276X-7-144.

[22] A.S. Silva, L. Diaz, S. Berberich, F.L. Deepak, M. Bañobre-lopez, Doxorubicin delivery performance of superparamagnetic carbon multi-core shell nanoparticles: pH dependence, stability and kinetic insight, Nanoscale (2022) 7220–7232, https://doi.org/10.1039/d1nr08550f.

[23] P. Biehl, M. von der Lühe, S. Dutz, F.H. Schacher, Synthesis, characterization, and applications of magnetic nanoparticles featuring polyzwitterionic coatings, Polymers 10 (no. 1) (2018), https://doi.org/10.3390/polym10010091.

[24] A.R.O. Rodrigues, I.T. Gomes, B.G. Almeida, J.P. Araújo, E.M.S. Castanheira, P.J.G. Coutinho, Magnetoliposomes based on nickel/silica core/shell nanoparticles: synthesis and characterization, Mater. Chem. Phys. 148 (3) (2014) 978–987, https://doi.org/10.1016/j.matchemphys.2014.09.008.

[25] M. Parashar, V.K. Shukla, R. Singh, Metal oxides nanoparticles via sol–gel method: a review on synthesis, characterization and applications, J. Mater. Sci. Mater. Electron. 31 (5) (2020) 3729–3749, https://doi.org/10.1007/s10854-020-02994-8.

[26] M. Niederberger, N. Pinna, Metal Oxide Nanoparticles in Organic Solvents, Synthesis, Formation, Assembly and Application, Springer, 2007, https://doi.org/10.1007/978-1-84882-671-7.

[27] A. Adamiano, M. Iafisco, A. Tampieri, Magnetic Core-Shell Nanoparticles, Elsevier Ltd, 2018, https://doi.org/10.1016/b978-0-08-102198-9.00009-0.

[28] V.F. Cardoso, A. Francesko, C. Ribeiro, M. Bañobre-López, P. Martins, S. Lanceros-Mendez, Advances in magnetic nanoparticles for biomedical applications, Adv. Healthcare Mater. 7 (5) (2018) 1–35, https://doi.org/10.1002/adhm.201700845.

[29] S. Uthaman, K.M. Huh, I.K. Park, Tumor microenvironment-responsive nanoparticles for cancer theragnostic applications, Biomater. Res. 22 (1) (2018) 1–11, https://doi.org/10.1186/s40824-018-0132-z.

[30] J. Liu, et al., Hollow mesoporous silica nanoparticles facilitated drug delivery via cascade pH stimuli in tumor microenvironment for tumor therapy, Biomaterials 83 (2016) 51–65, https://doi.org/10.1016/j.biomaterials.2016.01.008.

[31] J.R.P. Oliveira, et al., C, Carbon-Based Magnetic Nanocarrier for Controlled Drug Release: A Green Synthesis Approach 5 (1) (2019) 1, https://doi.org/10.3390/c5010001.

[32] R.O. Rodrigues, et al., Multifunctional graphene-based magnetic nanocarriers for combined hyperthermia and dual stimuli-responsive drug delivery, Mater. Sci. Eng. C 93 (2018) 206–217, https://doi.org/10.1016/j.msec.2018.07.060.

[33] A.S. Silva, et al., Doxorubicin delivery performance of superparamagnetic carbon multi-core shell nanoparticles: pH dependence, stability and kinetic insight, Nanoscale 14 (19) (2022) 7220–7232, https://doi.org/10.1039/D1NR08550F.

[34] A.S. Silva, et al., Hybrid multi-core shell magnetic nanoparticles for wet peroxide oxidation of paracetamol: application in synthetic and real matrices, J. Environ. Chem. Eng. (2023), 110806, https://doi.org/10.1016/j.jece.2023.110806.

[35] C.F. Thorn, et al., Doxorubicin pathways, Pharmacogenetics Genom. 21 (7) (2011) 440–446, https://doi.org/10.1097/fpc.0b013e32833ffb56.

[36] C.M. Lee, I.F. Tannock, Inhibition of endosomal sequestration of basic anticancer drugs: influence on cytotoxicity and tissue penetration, Br. J. Cancer 94 (6) (2006) 863–869, https://doi.org/10.1038/sj.bjc.6603010.

[37] M. Yu, C. Lee, M. Wang, I.F. Tannock, Influence of the proton pump inhibitor lansoprazole on distribution and activity of doxorubicin in solid tumors, Cancer Sci. 106 (10) (2015) 1438–1447, https://doi.org/10.1111/cas.12756.

[38] 5 - mathematical models of drug release, in: M.L. Bruschi (Ed.), Strategies to Modify the Drug Release from Pharmaceutical Systems, Woodhead Publishing, 2015, pp. 63–86, https://doi.org/10.1016/B978-0-08-100092-2.00005-9.

[39] A. Khan, M. Iqbal Ch, J. Khan, G. Majid Khan, M. Hanif, A. Khan, Formulation development and in vitro characterization of sustained release matrix tablets of verapamil HCl using synthetic and natural polymers, Lat. Am. J. Pharm. 34 (2) (2015) 277–282.

[40] T. Giannakopoulou, L. Kompotiatis, A. Kontogeorgakos, G. Kordas, Microwave behavior of ferrites prepared via sol-gel method, J. Magn. Magn Mater. 246 (3) (2002) 360–365, https://doi.org/10.1016/S0304-8853(02)00106-3.

[41] W.J. Liu, Y.X. Liu, X.Y. Yan, G.P. Yong, Y.P. Xu, S.M. Liu, One-pot synthesis of yolk-shell mesoporous carbon spheres with high magnetisation, J. Mater. Chem. A 2 (25) (2014) 9600–9606, https://doi.org/10.1039/c4ta01088d.

[42] D. Nath, F. Singh, R. Das, X-ray diffraction analysis by Williamson-Hall, Halder-Wagner and size-strain plot methods of CdSe nanoparticles- a comparative study, Mater. Chem. Phys. 239 (April 2019) (2020), 122021, https://doi.org/10.1016/j.matchemphys.2019.122021.

[43] J.L. Diaz De Tuesta, et al., Performance and modeling of Ni(II) adsorption from low concentrated wastewater on carbon microspheres prepared from tangerine peels by FeCl3-assisted hydrothermal carbonization, J. Environ. Chem. Eng. 10 (5) (2022), https://doi.org/10.1016/j.jece.2022.108143.

[44] F.F. Roman, et al., Carbon nanomaterials from polyolefin waste: effective catalysts for quinoline degradation through catalytic wet peroxide oxidation, Catalysts 13 (9) (Aug. 2023) 1259, https://doi.org/10.3390/catal13091259.

[45] J.L. Diaz de Tuesta, A.M.T. Silva, J.L. Faria, H.T. Gomes, Removal of Sudan IV from a simulated biphasic oily wastewater by using lipophilic carbon adsorbents, Chem. Eng. J. 347 (April) (2018) 963–971, https://doi.org/10.1016/j.cej.2018.04.105.

[46] D.Y. Li, Y.K. Sun, P.Z. Gao, X.L. Zhang, H.L. Ge, Structural and magnetic properties of nickel ferrite nanoparticles synthesized via a template-assisted sol-gel method, Ceram. Int. 40 (PB) (2014) 16529–16534, https://doi.org/10.1016/j.ceramint.2014.08.006.

[47] C. Cherpin, D. Lister, F. Dacquait, L. Liu, Study of the solid-state synthesis of nickel ferrite (NiFe2O4) by X-ray diffraction (XRD), scanning electron microscopy (SEM) and Raman spectroscopy, Materials 14 (no. 10) (2021), https://doi.org/10.3390/ma14102557.

[48] R. Sen, P. Jain, R. Patidar, S. Srivastava, R.S. Rana, N. Gupta, Synthesis and characterization of nickel ferrite (NiFe2O4) nanoparticles prepared by sol- gel method, Mater. Today Proc 2 (4–5) (2015) 3750–3757, https://doi.org/10.1016/j.matpr.2015.07.165.

[49] W.A. Khoso, N. Haleem, M.A. Baig, Y. Jamal, Synthesis, characterization and heavy metal removal efficiency of nickel ferrite nanoparticles (NFN's), Sci. Rep. 11 (1) (2021) 1–10, https://doi.org/10.1038/s41598-021-83363-1.

[50] F.H. Chen, L.M. Zhang, Q.T. Chen, Y. Zhang, Z.J. Zhang, Synthesis of a novel magnetic drug delivery system composed of doxorubicin-conjugated Fe3O4 nanoparticle cores and a PEG-functionalized porous silica shell, Chem. Commun. 46 (45) (2010) 8633–8635, https://doi.org/10.1039/c0cc02577a.

[51] S.P. Schwaminger, D. Bauer, P. Fraga-García, F.E. Wagner, S. Berensmeier, Oxidation of magnetite nanoparticles: impact on surface and crystal properties, CrystEngComm 19 (2) (2017) 246–255, https://doi.org/10.1039/c6ce02421a.

[52] B. Ankamwar, Size and shape effect on biomedical applications of nanomaterials, Biomed. Eng. - Tech. Appl. Med. (2012) 20–40, https://doi.org/10.5772/46121.

[53] J. Singh, et al., Highly efficient bienzyme functionalized biocompatible nanostructured nickel ferrite-chitosan nanocomposite platform for biomedical application, J. Phys. Chem. C 117 (16) (2013) 8491–8502, https://doi.org/10.1021/jp312698g.

[54] T. Ruthradevi, et al., Investigations on nickel ferrite embedded calcium phosphate nanoparticles for biomedical applications, J. Alloys Compd. 695 (2017) 3211–3219, https://doi.org/10.1016/j.jallcom.2016.11.300.

[55] X. Lasheras, et al., Chemical synthesis and magnetic properties of monodisperse nickel ferrite nanoparticles for biomedical applications, J. Phys. Chem. C 120 (6) (2016) 3492–3500, https://doi.org/10.1021/acs.jpcc.5b10216.

[56] P. Sivakumar, R. Ramesh, A. Ramanand, S. Ponnusamy, C. Muthamizhchelvan, Synthesis and characterization of nickel ferrite magnetic nanoparticles, Mater. Res. Bull. 46 (12) (2011) 2208–2211, https://doi.org/10.1016/j.materresbull.2011.09.009.

[57] R.B. Kamble, V. Varade, K.P. Ramesh, V. Prasad, Domain size correlated magnetic properties and electrical impedance of size dependent nickel ferrite nanoparticles, AIP Adv. 5 (1) (2015), https://doi.org/10.1063/1.4906101.

[58] A.B. Mapossa, J. Dantas, M.R. Silva, R.H.G.A. Kiminami, A.C.F.M. Costa, M. O. Daramola, Catalytic performance of NiFe2O4 and Ni0.3Zn0.7Fe2O4 magnetic nanoparticles during biodiesel production, Arab. J. Chem. 13 (2) (2020) 4462–4476, https://doi.org/10.1016/j.arabjc.2019.09.003.

[59] J.L. Diaz de Tuesta, F.V.M. de Almeida, J.R.P. Oliveira, P. Praça, M.C. Guerreiro, H. T. Gomes, Kinetic insights on wet peroxide oxidation of caffeine using EDTA-functionalized low-cost catalysts prepared from compost generated in municipal solid waste treatment facilities, Environ. Technol. Innov. 24 (2021), 101984, https://doi.org/10.1016/j.eti.2021.101984.

[60] J.L. Diaz De Tuesta, et al., Assisted hydrothermal carbonization of agroindustrial byproducts as effective step in the production of activated carbon catalysts for wet peroxide oxidation of micro-pollutants, J. Environ. Chem. Eng. 9 (1) (2021), 105004, https://doi.org/10.1016/j.jece.2020.105004.

[61] R.O. Rodrigues, et al., Multifunctional graphene-based magnetic nanocarriers for combined hyperthermia and dual stimuli-responsive drug delivery, Mater. Sci. Eng. C 93 (2018) 206–217, https://doi.org/10.1016/j.msec.2018.07.060.

[62] M. Shamsi, A. Sedaghatkish, M. Dejam, M. Saghafian, M. Mohammadi, A. Sanati-Nezhad, Magnetically assisted intraperitoneal drug delivery for cancer chemotherapy, Drug Deliv. 25 (1) (2018) 846–861, https://doi.org/10.1080/10717544.2018.1455764.

[63] B. Shapiro, S. Kulkarni, A. Nacev, S. Muro, P.Y. Stepanov, I.N. Weinberg, Open challenges in magnetic drug targeting, Wiley Interdiscip. Rev. Nanomedicine Nanobiotechnology 7 (3) (2015) 446–457, https://doi.org/10.1002/wnan.1311.

[64] S. Kralj, T. Potrc, P. Kocbek, S. Marchesan, D. Makovec, Design and fabrication of magnetically responsive nanocarriers for drug delivery, Curr. Med. Chem. 24 (5) (2017) 454–469.

[65] L. Ao, et al., Polydopamine-derived hierarchical nanoplatforms for efficient dual-modal imaging-guided combination in vivo cancer therapy, ACS Appl. Mater. Interfaces 10 (15) (2018) 12544–12552, https://doi.org/10.1021/acsami.8b02973.

[66] Y.P. Wang, et al., Trifunctional Fe3O4/CaP/alginate core-shell-corona nanoparticles for magnetically guided, pH-responsive, and chemically targeted chemotherapy, ACS Biomater. Sci. Eng. 3 (10) (2017) 2366–2374, https://doi.org/10.1021/acsbiomaterials.7b00230.

[67] H. Wan, H. Qin, Z. Xiong, W. Zhang, H. Zou, Facile synthesis of yolk-shell magnetic mesoporous carbon microspheres for efficient enrichment of low abundance peptides, Nanoscale 5 (22) (2013) 10936–10944, https://doi.org/10.1039/c3nr02932h.

[68] M. Thommes, et al., Physisorption of gases, with special reference to the evaluation of surface area and pore size distribution (IUPAC Technical Report), Pure Appl. Chem. 87 (9–10) (2015) 1051–1069, https://doi.org/10.1515/pac-2014-1117.

[69] X. Wang, S. Li, G. Yang, C. Jin, S. Huang, Insights into the resorcinol-formaldehyde resin coating process focusing on surface modification of colloidal SiO2 particles, Langmuir 36 (10) (2020) 2654–2662, https://doi.org/10.1021/acs.langmuir.9b03595.

[70] G.N. Lucena, et al., Drug delivery and magnetic hyperthermia based on surface engineering of magnetic nanoparticles, Magn. Nanoparticles Hum. Heal. Med. Curr. Med. Appl. Altern. Ther. Cancer (2021) 231–249.

[71] A. Hervault, et al., Doxorubicin loaded dual pH- and thermo-responsive magnetic nanocarrier for combined magnetic hyperthermia and targeted controlled drug delivery applications, Nanoscale 8 (24) (2016) 12152–12161, https://doi.org/10.1039/c5nr07773g.

[72] S. Bagherifam, et al., PH-responsive Nano carriers for doxorubicin delivery, Pharm. Res. (N. Y.) 32 (4) (2015) 1249–1263, https://doi.org/10.1007/s11095-014-1530-0.

[73] T. Vrbanec, P. Šket, F. Merzel, M. Smrkolj, J. Grdadolnik, Spectroscopic characterization of omeprazole and its salts, J. Spectrosc. (Figure 1) (2017) 2017, https://doi.org/10.1155/2017/6505706.

[74] R. Yang, S.G. Schulman, P.J. Zavala, Acid-base chemistry of omeprazole in aqueous solutions, Anal. Chim. Acta 481 (1) (2003) 155–164, https://doi.org/10.1016/S0003-2670(03)00076-X.

[75] C. Zhuang, C. Shi, F. Tao, Y. Cui, Honeycomb structural composite polymer network of gelatin and functional cellulose ester for controlled release of omeprazole, Int. J. Biol. Macromol. 105 (2017) 1644–1653, https://doi.org/10.1016/j.ijbiomac.2017.01.019.

[76] D. Huang, et al., Polyurethane/doxorubicin nanoparticles based on electrostatic interactions as pH-sensitive drug delivery carriers, Polym. Int. 67 (9) (2018) 1186–1193, https://doi.org/10.1002/pi.5618.

[77] G. Unsoy, R. Khodadust, S. Yalcin, P. Mutlu, U. Gunduz, Synthesis of Doxorubicin loaded magnetic chitosan nanoparticles for pH responsive targeted drug delivery, Eur. J. Pharm. Sci. 62 (2014) 243–250, https://doi.org/10.1016/j.ejps.2014.05.021.

[78] S. Guo, D. Li, L. Zhang, J. Li, E. Wang, Monodisperse mesoporous superparamagnetic single-crystal magnetite nanoparticles for drug delivery, Biomaterials 30 (10) (2009) 1881–1889, https://doi.org/10.1016/j.biomaterials.2008.12.042.

[79] F. Wang, et al., Facile solvothermal synthesis of monodisperse superparamagnetic mesoporous Fe3O4 nanospheres for pH-responsive controlled drug delivery, Colloids Surfaces A Physicochem. Eng. Asp. 622 (April) (2021), 126643, https://doi.org/10.1016/j.colsurfa.2021.126643.

[80] C. Dey, A. Ghosh, M. Ahir, A. Ghosh, M.M. Goswami, Improvement of anticancer drug release by cobalt ferrite magnetic nanoparticles through combined pH and

temperature responsive technique, ChemPhysChem 19 (21) (2018) 2872–2878, https://doi.org/10.1002/cphc.201800535.

[81] Y. Gao, et al., In vitro release kinetics of antituberculosis drugs from nanoparticles assessed using a modified dissolution apparatus, BioMed Res. Int. 2013 (2013), https://doi.org/10.1155/2013/136590.

[82] A.R. Fernandes, J. Dias-Ferreira, C. Cabral, M.L. Garcia, E.B. Souto, Release kinetics and cell viability of ibuprofen nanocrystals produced by melt-emulsification, Colloids Surfaces B Biointerfaces 166 (2018) 24–28, https://doi.org/10.1016/j.colsurfb.2018.03.005.